Shi *et al. Chem Synth* 2024;4:45
DOI: 10.20517/cs.2023.68

Chemical Synthesis

Research Article

Open Access

A novel structure Ti/Fe_2O_3/Cu_2S/$Co(OH)_x$ enhances the photoelectrochemical water splitting performance of iron oxide

Hao-Yan Shi[1,2,3], Yan-Xin Chen[1,2,3,4,*], Ming-Hao Ji[1,3], Qian-Qian Zhou[1,3], Ke-Xian Li[1,3], Hai-Long Wang[1,3], Rui Chen[1,3], Xiu-Mei Lin[5,*], Can-Zhong Lu[1,2,3,4,*]

[1]State Key Laboratory of Structural Chemistry, Fujian Institute of Research on the Structure of Matter, Chinese Academy of Sciences, Fuzhou 350002, Fujian, China.
[2]School of Chemical Sciences, University of Chinese Academy of Sciences, Beijing 100049, China.
[3]Xiamen Key Laboratory of Rare Earth Photoelectric Functional Materials, Xiamen Institute of Rare-earth Materials, Haixi Institutes, Chinese Academy of Sciences, Xiamen 361021, Fujian, China.
[4]Fujian Science & Technology Innovation Laboratory for Optoelectronic Information of China, Fuzhou 350108, Fujian, China.
[5]College of Chemistry, Chemical Engineering and Environment, Fujian Province University Key Laboratory of Analytical Science, Minnan Normal University, Zhangzhou 363000, Fujian, China.

[*]**Correspondence to:** Prof. Yan-Xin Chen, Prof. Can-Zhong Lu, State Key Laboratory of Structural Chemistry, Fujian Institute of Research on the Structure of Matter, Chinese Academy of Sciences, 155 Yangqiao Road West, Fuzhou 350002, Fujian, China. E-mail: yanxinchen@fjirsm.ac.cn; czlu@fjirsm.ac.cn; Dr. Xiu-Mei Lin, College of Chemistry, Chemical Engineering and Environment, Fujian Province University Key Laboratory of Analytical Science, Minnan Normal University, 36 Xianqian Street, Zhangzhou 363000, Fujian, China. E-mail: xiu-mei.lin@xmu.edu.cn

How to cite this article: Shi HY, Chen YX, Ji MH, Zhou QQ, Li KX, Wang HL, Chen R, Lin XM, Lu CZ. A novel structure Ti/Fe_2O_3/Cu_2S/$Co(OH)_x$ enhances the photoelectrochemical water splitting performance of iron oxide. *Chem Synth* 2024;4:45. https://dx.doi.org/10.20517/cs.2023.68

Received: 22 Dec 2023 **First Decision:** 16 Apr 2024 **Revised:** 25 Jun 2024 **Accepted:** 5 Jul 2024 **Published:** 7 Aug 2024

Academic Editor: Aicheng Chen **Copy Editor:** Pei-Yun Wang **Production Editor:** Pei-Yun Wang

Abstract

The slow oxygen evolution kinetics of iron oxide nanorod arrays have limited their applications in photocatalytic water splitting. Herein, we introduce p-type semiconductor cuprous oxide and further cover cobalt hydroxide ultrathin nanosheets on the surface of both by electrochemical deposition; these methods obviously enhanced the photoelectrochemical (PEC) water splitting performance of iron oxide nanorods on titanium sheet substrate. The photocurrent of this heterostructure reached 4.8 mA/cm^2 at 1.23 V (*vs.* reversible hydrogen electrode) in a 1 M KOH aqueous solution under AM 1.5G illumination, which is much higher than the currently reported photocatalytic water splitting performance of iron oxide nanoarrays. The construction of Fe_2O_3/Cu_2S p-n heterojunction accelerates the separation of photogenerated carriers in the main body of Fe_2O_3 nanorod arrays; as an excellent oxygen evolution catalyst (OEC), the introduction of $Co(OH)_x$ accelerates the kinetic process of interfacial water oxidation leading to the rapid depletion of photogenerated holes, which further improves the charge separation on the photoanode surface. Thus, the synergistic effect between Fe_2O_3/Cu_2S p-n heterojunctions and oxygen evolution catalysts enhanced the iron oxide nanorod array photoanodes.

Keywords: $Ti/Fe_2O_3/Cu_2S/Co(OH)_x$, photoelectrochemical, water splitting, hydrogen evolution

INTRODUCTION

With economic and social development, the energy and environmental crises are increasingly becoming a constraint on human progress[1], but the photoelectrochemical (PEC) water splitting into hydrogen[2] offers a promising solution that exploits nature's most abundant solar energy to decompose the earth's vastly more abundant water resources into clean, environmentally friendly, and highly energy-dense hydrogen[3]. In 1972, Fujishima and Honda demonstrated the potential of titanium dioxide (TiO_2)[4] semiconductor materials in splitting water into hydrogen and oxygen in photochemical cells[5].

Many highly active photoanodes have been reported, such as a monoclinic tungsten trioxide (WO_3) nanowire by Nayak *et al.*[6]. The PEC activity of this nanowire was about 21 times higher than that of WO_3-H_2O nanoplates and higher than that of the existing WO_3 nanostructures. The enhanced PEC activity is attributed to the one-dimensional morphology of the WO_3 nanowires, larger surface area, and other factors.

Among the numerous semiconductor photoelectric anode materials, hematite[7] (α-Fe_2O_3) has become one of the most widely applied photoanode materials at this stage because of its excellent stability and environmental friendliness[8,9]. Fe_2O_3 has a band gap (E_g) of 1.9 to 2.2 eV[10]. Therefore, its light absorption range exceeds 600 nm, and it has sufficient visible light absorption[11]; theoretical calculations show that an ideal Fe_2O_3 photoanode can achieve up to 12.6 mA/cm^2 at 1.23 V [*vs.* reversible hydrogen electrode (RHE)] under 100 mW/cm^2 (AM 1.5G) of solar radiation[12]. However, the actual performance of Fe_2O_3 in PEC cells falls significantly below the theoretical value due to fast carrier complexation and a short hole diffusion length (only 2-4 nm), which severely affects its practical application[8]. Various modification strategies have been used to alleviate the shortcomings of hematite, such as doping[13], homojunction[14]/heterojunction[15] formation, and surface modification[16].

Cu_2S is a widely utilized p-type semiconductor commonly employed in solar energy conversion[17]. It has an excellent ability to absorb light utilizing a wide range of wavelengths[18], while its high conductivity permits efficient photogenerated charge transfer[19]. A recent report has shown that the heterostructure formed by Fe_2O_3 and Cu_2S exhibits enhanced photocatalytic activity under oxygen evolution reaction (OER). The enhanced activity is attributed to the formation of covalent bonds between Cu_2S and Fe_2O_3, particularly the S–O bonds[20].

The construction of p-n junctions has been shown to optimize the PEC performance of photoanode arrays[21]. The built-in electric field facilitates the rapid separation of photogenerated carriers at the p-n junction[22] interface. It reduces bulk phase complexation, thereby enhancing the PEC water-splitting performance of the photoanode[23]. For instance, using the Ar plasma-assisted strategy, Meng *et al.* fabricated a SnS_2 nanosheet array with numerous surface holes[24]. The reduction property of Ar atoms led to a partial reduction of Sn^{4+} to Sn^{2+}, forming a SnS/SnS_2 p-n junction of the nanosheet array. This facilitates carrier separation and prolongs carrier lifetime. As a result, the photocurrent density of this nanosheet array was 2.15 mA/cm^2. In addition, Wu *et al.* also synthesized atomic sandwiched nitrogen-doped SnS_2

nanosheets (p-n-p-SnS_2) by controlled NH_3 treatment[25]. The best sample achieved an optical current density of 3.28 mA/cm^2. The outstanding performance can be attributed to the formation of p-n-p junctions that facilitate electron-hole transfer and optimize the kinetics of the oxygen precipitation reaction. Notably, loaded oxygen precipitation catalysts [oxygen evolution catalysts (OECs)] are considered a particularly effective method for enhancing the surface reaction kinetics of α-Fe_2O_3 membranes[26]. The OECs used in PEC systems are usually derived from superior electrocatalysts, and many of these low-cost transition-metal-based OECs have been shown to be able to achieve low overpotentials for electrochemical OER[27].

The construction of ternary photocatalytic or PEC materials has been widely studied. For example, Yang *et al.* reported a photocatalyst TiO_2/$MgTiO_3$/C that was synthesized at the gram scale by a simple mechanochemical method[28]. The ternary heterostructure achieves excellent light utilization and good photostability and is more conducive to solar-driven photochemical hydrogen production. An *et al.* achieved the co-synthesis of H_2O_2 and hydrogen by constructing a ternary photoanode $CaSnO_3$/$SrTiO_3$/$BiVO_4$ (CSO/STO/BVO), replacing the four-electron reaction with the kinetically superior two-electron reaction optimized the kinetics of the water oxidation of the PEC and facilitated the separation of the products[29]. In addition, the authors performed outdoor tests and considered issues for practical engineering applications.

However, simultaneous improvement in charge separation and surface oxygen precipitation kinetics at α-Fe_2O_3 nanorod array photoanodes through synergistic effects between p-n heterojunctions and OECs has not yet been achieved.

Herein, we grew an array of Fe_2O_3 nanorods on titanium sheets using a hydrothermal method, which was used as a photoanode named Ti/Fe_2O_3. Further, we introduced a p-type semiconductor cuprous sulfide to form a p-n heterojunction photoanode (named Ti/Fe_2O_3/Cu_2S), which significantly enhanced the PEC water-oxidation performance of the photoanode. In addition, the surfaces of both were further covered with ultrathin nanosheets of cobalt hydroxide by electrochemical deposition, which also significantly improved the PEC water decomposition performance of the Ti/Fe_2O_3/Cu_2S photoanode. The photocurrent of this heterostructure [named Ti/Fe_2O_3/Cu_2S/$Co(OH)_x$] reached 4.8 mA/cm^2 at 1.23 V (*vs.* RHE) in 1 M KOH aqueous solution at AM 1.5G, which is much higher than the PEC water splitting performance of the Fe_2O_3 nanoarrays reported so far. The substantial improvement of the catalytic performance is mainly attributed to two points: one is that the introduction of Fe_2O_3/Cu_2S p-n heterojunction accelerates the separation of photogenerated carriers in the Fe_2O_3 nanorod arrays; the other is that the addition of OEC on the $Co(OH)_x$ surface accelerates the kinetics of the interfacial water oxidation, and the rapid depletion of the photogenerated holes further improves the photo-anodic surface charge separation. Therefore, the synergistic effect between Fe_2O_3/Cu_2S p-n heterojunction and OEC significantly enhances the PEC water decomposition performance of the iron oxide nanorod array photoanode.

EXPERIMENTAL

Materials and synthesis methods

All chemical reagents used were analytically pure and underwent no further refinement during the experiment, including titanium foil, concentrated hydrochloric acid, acetone (C_3H_6O), ethanol absolute (C_2H_6O), deionized water, $FeCl_3·6H_2O$, $NaNO_3$, $Co(NO_3)_2·6H_2O$, CuCl, and $Na_2S·9H_2O$.

Preparation of Ti/Fe_2O_3 photoanode

The Ti/Fe_2O_3 nanorod photoelectrode was prepared by a simple hydrothermal method[7] [Figure 1]. Firstly, 182.4 mg of $FeCl_3·6H_2O$ and 383 mg of $NaNO_3$ were dissolved in 4.5 mL of ultrapure water, and the

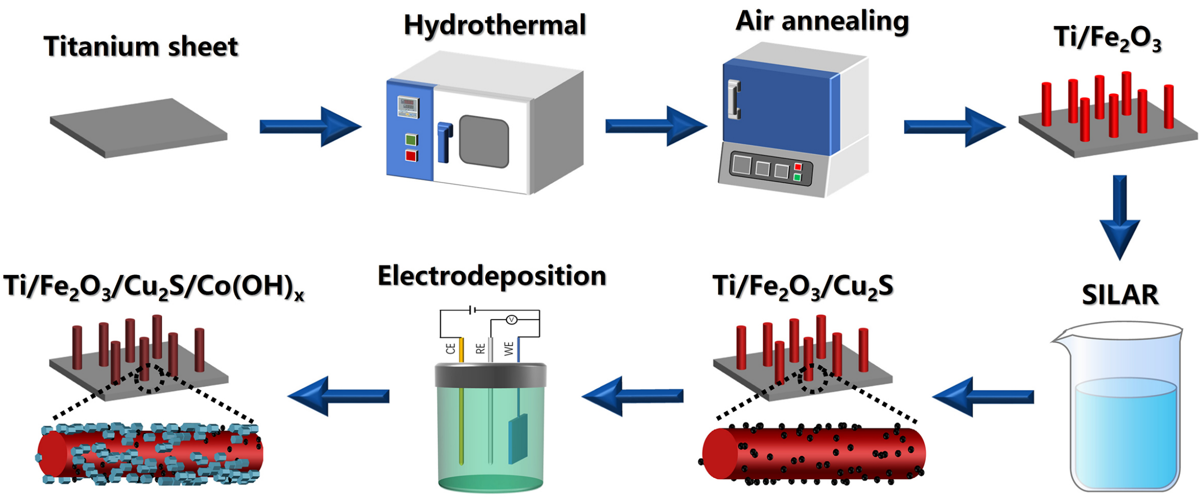

Figure 1. Synthesis steps of $Ti/Fe_2O_3/Cu_2S/Co(OH)_x$ photoanode.

resulting solution was stirred continuously for 2 h before adding 20 μL concentrated hydrochloric acid. Next, the prepared mixed solution of 0.15 M $FeCl_3$ and 1 M $NaNO_3$ was transferred to the stainless steel autoclave lined with polytetrafluoroethylene, and the titanium sheet was also immersed in the solution. After that, the autoclave was put into the oven and heated at 100 °C (1 °C/min) for 5 h. After the reaction, the titanium sheet was deposited with a uniform yellow β-FeOOH layer. Finally, the substrate was washed with deionized water to remove residual FeOOH and calcined at 550 °C (2 °C/min) for 2 h to obtain a sample called Ti/Fe_2O_3. The titanium sheets used in the hydrothermal reaction were ultrasonically cleaned in advance with a mixture of hydrochloric acid, ethanol acetone, and deionized water for 0.5 h to remove organic pollutants and dust.

Preparation of $Ti/Fe_2O_3/Cu_2S$ photoanode

According to previous reports, $Ti/Fe_2O_3/Cu_2S$ heterostructures were synthesized using the successive ion layer adsorption and reaction (SILAR) method[18] [Figure 1]. The α-Fe_2O_3 nanorod photoelectrode was first immersed in a CuCl-saturated solution for 60 s, which allowed Cu^+ to adsorb on the surface of the α-Fe_2O_3 nanorod photoelectrode. Then, the photoelectrode was rinsed in deionized water for 60 s to prevent excessive Cu_2S precipitation. Afterward, the photoelectrode was immersed in 5 mM Na_2S anion solution for 60 s to react S^{2-} with adsorbed Cu^+ to produce Cu_2S. Finally, the photoelectrode was rinsed with deionized water for 60 s. These steps constitute a cycle count. The photoelectrode was immersed in the solution for different cycles (3, 5, 10, 15) to control the deposition amount of Cu_2S. Finally, the photoelectrode synthesized by the SILAR method was annealed in an argon atmosphere at 200 °C (5 °C/min) for 2 h, resulting in a sample called $Ti/Fe_2O_3/Cu_2S$.

Preparation of $Ti/Fe_2O_3/Cu_2S/Co(OH)_x$ photoanode

According to previous reports[27], the photoelectrode $Ti/Fe_2O_3/Cu_2S/Co(OH)_x$ was synthesized through a simple electrochemical deposition method [Figure 1]. Using a 1 mA/cm² cathode current density, $Ti/Fe_2O_3/Cu_2S$ photoelectrode was deposited onto ultra-thin $Co(OH)_x$ nanosheets in a solution containing 2 mM $Co(NO_3)_2$. The best performance of the photoelectrode could be achieved by selecting different deposition times (30, 60, 90, and 120 s). The final sample obtained was called $Ti/Fe_2O_3/Cu_2S/Co(OH)_x$.

Preparation of Cu_2S nanoparticles

The saturated CuCl and 5 mM Na_2S solutions were mixed with thorough stirring, and the Cu_2S nanoparticles were obtained after pumping and filtering. After acid washing and centrifugation, the obtained Cu_2S nanoparticles were deposited on fluorine-doped tin oxide (FTO) by spin coating for electrochemical testing.

Materials characterizations

The microscopic morphology was evaluated using a scanning electron microscope (SEM, Apreo S LoVac, Thermo Fisher Scientific) with an operating voltage of 10 kV. The TF20 (FEI), operated at 200 kV, was used to perform transmission electron microscopy (TEM) and selected area electron diffraction (SAED) techniques to characterize the detailed morphology, size, and element composition of the samples. The crystal structure of the sample was described using X-ray diffraction (XRD) data obtained from the Miniflex 600 X-ray diffractometer. The measurement range was 20°-80° with CuK radiation. The light absorption ability of the sample was evaluated by collecting the ultraviolet-visible (UV-vis) absorption spectrum using the Cary 5000 spectrophotometer (Agilent). X-ray photoelectron spectroscopy (XPS) was performed with Al Ka rays.

The bandgap energy (E_g) is determined from UV-vis diffuse reflectance spectroscopy (UV-vis-DRS), specifically utilizing the Tauc diagram. E_g is calculated using:

$$(ah\nu)^{x} = A\left(h\nu - E_g\right) \tag{1}$$

Which represents Tauc plotting, where a is the direct light absorption coefficient, h is Planck's constant, ν is the frequency of the incident light, A is the proportionality constant, and E_g is the energy gap of the semiconductor photocatalyst. For direct bandgap semiconductors, x equals 2; for indirect bandgap semiconductors, x equals 1/2.

PEC measurements

The PEC test was conducted using a PEC2000 PEC test system (Beijing Perfectlight Technology Co., Ltd., Beijing, China), which comprises a Shanghai Chenhua electrochemical workstation (CHI760e), a xenon lamp (PLS-FX300HU, Beijing Perfectlight) with an AM 1.5G filter (100 mW/cm^2), a chopper module (PFS40A shutter actuator), and a single-room electrochemical cell. The PEC tests were conducted under no light, light, or alternating light conditions. Linear sweep voltammetry (LSV) typically measured the potential range between -0.31 and 0.61 V (*vs.* Ag/AgCl), with light intermittently blocked by a shutter toggling every 5 s. Chronoamperometric testing (I-t) was performed at 0.23 V (*vs.* Ag/AgCl) under light conditions. The prepared photoelectric electrode served as the working electrode, a Pt plate as the counter electrode, Ag/AgCl (saturated KCl) as the reference electrode, and 1 M KOH (pH = 13.6) as the electrolyte. Throughout the testing, it was ensured that the working electrode had a light-exposed area of 1 cm^2. The measured potential could be converted to E_{RHE} (V) value using:

$$E_{RHE} = E_{Ag/AgCl} + 0.0592 \times pH + E^{0}_{Ag/AgCl} \tag{2}$$

Where $E^{0}_{Ag/AgCl}$ = 0.1976 V *vs.* RHE (25 °C).

The applied bias photon-to-current efficiency (ABPE) with external bias can be calculated using:

$$ABPE(\%) = \frac{J_{ph} \times \left(1.23\ V - E_{app}\right)}{P_{light}} \times 100\% \tag{3}$$

Where J_{ph} denotes the photocurrent density (mA/cm^2) measured by the electrochemical workstation. E_{app} signifies the relationship between the applied bias voltage and E_{RHE} (V), and P_{light} represents the total light intensity of AM 1.5G (100 mW/cm^2).

The incident monochromatic photon electron conversion efficiency (IPCE) and Mott-Schottky (MS) measurements were conducted in the IPCE1000 PEC testing system (Beijing Perfectlight Technology Co., Ltd., Beijing, China). The instrument is equipped with an electrochemical workstation (CS 350H, Wuhan Kotex Instruments Co., Ltd., China). IPCE can be calculated by:

$$IPCE(\%) = 1240 \times [I_{ph}/(\lambda \times P_{in})] \times 100\% \tag{4}$$

Where I_{ph} (A/cm^2) refers to the output photocurrent density at each wavelength (λ, nm), and P_{in} represents the incident light power density. Usually, the IPCE spectrum is calculated based on the photocurrent density recorded by the chronoamperometric method. The incident monochromatic light of 300-600 nm is separated by a monochromator using a xenon lamp (PLS-FX300HU, Beijing Perfectlight).

The MS measurement results were used to illustrate the flat band potentials. The frequency range of the electrochemical analyzer is 0.1~100,000 Hz. The working electrodes were measured at 500, 1,000, 1,500, and 2,000 Hz, respectively. Based on the MS plot, the flat band potential of the photoelectrode can be determined according to:

$$\frac{1}{C^2} = \frac{2}{\mathrm{e}\varepsilon_0\varepsilon N_D}\left[(E - E_{FB}) - \frac{\kappa T}{\mathrm{e}}\right] \tag{5}$$

Where C is the space charge capacitance, e is the electron charge, ε is the vacuum permittivity (8.85×10^{-12} F·m^{-1}), ε_0 is the relative permittivity of hematite ($\varepsilon_0 = 80$), N_D is the charge donor density, which, in this case, can refer to the carrier concentration (cm^{-3}), E is the electrode applied potential, E_{FB} is the flat charged potential, κ is the Boltzmann constant (1.38×10^{-23} J·K^{-1}), and T is the absolute temperature (K).

The carrier concentration (N_D) of the obtained photoanode can be roughly estimated by:

$$N_D = \frac{2}{\mathrm{e}\varepsilon_0\varepsilon}\left[\frac{d\left(\frac{1}{C^2}\right)}{dE}\right]^{-1} \tag{6}$$

Electrochemical impedance spectroscopy (EIS) was performed using a Squidstat Plus electrochemical workstation (Admiral Instruments, Tempe, Arizona, USA).

PEC H_2 evolution experiments were conducted using an all-glass automatic online trace gas analysis system (Labsolar-6A, Beijing Perfectlight). The system utilized a xenon lamp (Microsolar 300, Beijing Perfectlight). This setup was interfaced with a commercial electrochemical workstation (Squidstat Plus, Admiral Instruments, Arizona) for bias voltage application (0.23 V *vs.* Ag/AgCl) and photocurrent data collection. The electrolyte used was a 1 M KOH solution (75 mL). Periodic analysis of PEC-generated H_2 was performed using a FULI-GC-9790II gas chromatograph (GC) (Zhejiang Fuli) equipped with a thermal conductivity detector (TCD), with argon (Ar) serving as the carrier gas at a flow rate of 30 mL/min.

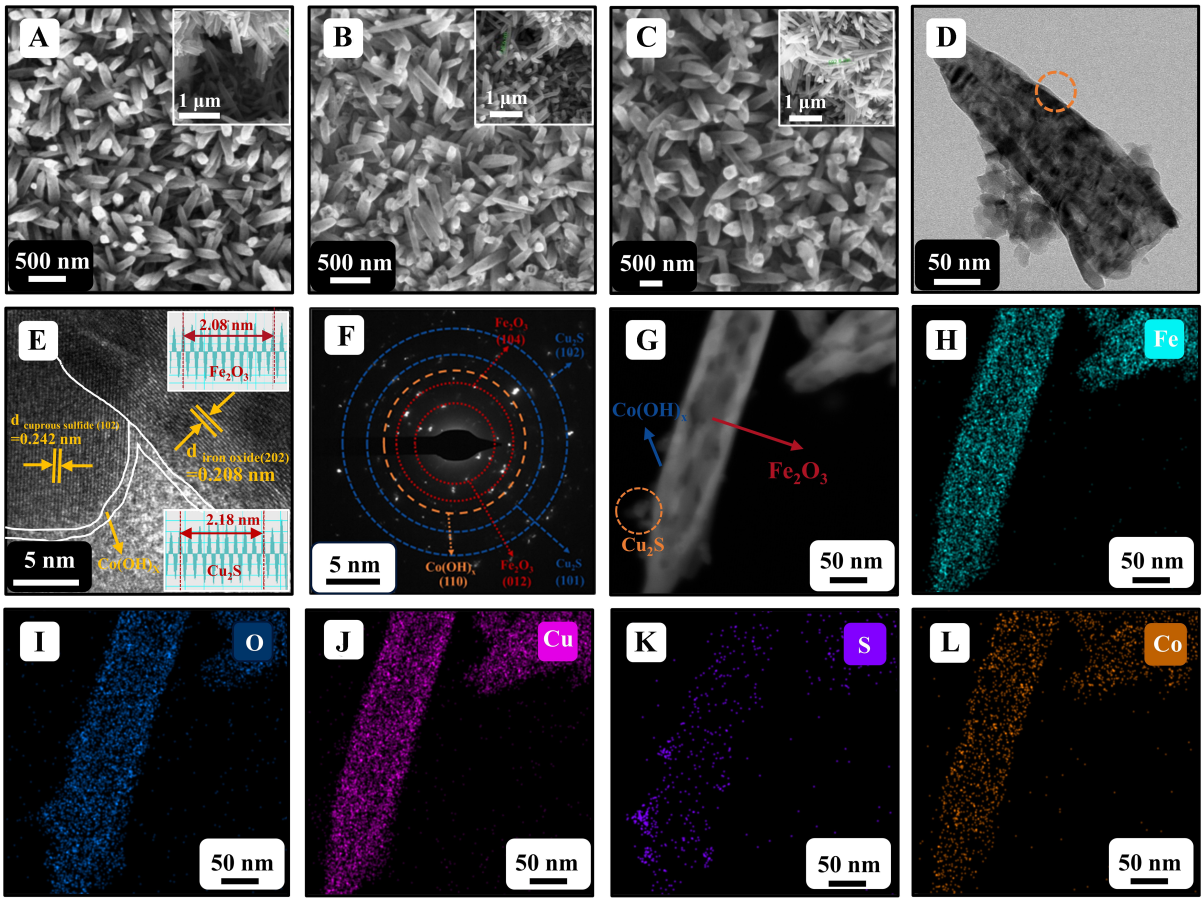

Figure 2. (A-C) SEM images of Ti/Fe_2O_3, Ti/Fe_2O_3/Cu_2S, and Ti/Fe_2O_3/Cu_2S/$Co(OH)_x$ photoanodes; (D and E) HRTEM images of Ti/Fe_2O_3/Cu_2S/$Co(OH)_x$ photoanode; (F) SAED images of Ti/Fe_2O_3/Cu_2S/$Co(OH)_x$ photoanode; (G) STEM image of Ti/Fe_2O_3/Cu_2S/$Co(OH)_x$ photoanode; (H-L) EDS mapping (Fe, O, Cu, S and Co) of Ti/Fe_2O_3/Cu_2S/$Co(OH)_x$ photoanode. SEM: Scanning electron microscope; HRTEM: high-resolution transmission electron microscopy; SAED: selected area electron diffraction; STEM: scanning transmission electron microscopy; EDS: energy dispersive spectroscopy.

RESULTS AND DISCUSSION

Morphology and structure

Ti/Fe_2O_3, Ti/Fe_2O_3/Cu_2S, and Ti/Fe_2O_3/Cu_2S/$Co(OH)_x$ photoanodes exhibit a semi-collapsed rod-shaped structure [Figure 2A-C], belonging to one-dimensional nanomaterials. The side view shows that the length of these rods is approximately 700 nm. Compared to Ti/Fe_2O_3, there is no obvious Cu_2S and $Co(OH)_x$ on the surface of Ti/Fe_2O_3/Cu_2S and Ti/Fe_2O_3/Cu_2S/$Co(OH)_x$ photoanodes, which may be due to the relatively small loading amount of Cu_2S and the deposition amount of $Co(OH)_x$. By increasing the loading of Cu_2S, it was demonstrated that Cu_2S nanoparticles were synthesized, as detailed in Supplementary Figure 1. The rod-like structure of the Ti/Fe_2O_3/Cu_2S/$Co(OH)_x$ photoanode is observed by TEM [Figure 2D]; in Figure 2E, the calculated lattice spacing is compared with the XRD standard spectrum, demonstrating that the (102) crystal plane of Cu_2S is on the left of the figure[30], while the (202) crystal plane of Fe_2O_3 is on the right. In the high-resolution mode[31], a phase interface between Fe_2O_3 and Cu_2S is observed, with a heterojunction structure forming between the two. In addition, an ultra-thin $Co(OH)_x$ film outside the Fe_2O_3 and Cu_2S heterojunction structure wraps both, forming a $Co(OH)_x$-covered p-Cu_2S/n-Fe_2O_3 structure.

The SAED characterization results are shown in Figure 2F. The SAED profiles correspond to the (001) and (002) crystal faces in Cu_2S and (010) crystal face in $Co(OH)_x$, which are the main peaks of Cu_2S and $Co(OH)_x$ crystals, respectively; this further proves that the presence of Cu_2S and $Co(OH)_x$ nanorods in $Ti/Fe_2O_3/Cu_2S/Co(OH)_x$ nanorods $Co(OH)_x$. In addition, the SAED pattern corresponds to the (300) and (006) crystal faces in the α-Fe_2O_3 crystals, which are the main peaks of α-Fe_2O_3, further proving that the main component of the $Ti/Fe_2O_3/Cu_2S/Co(OH)_x$ nanorods is α-Fe_2O_3. Energy dispersive spectroscopy (EDS) surface scan characterization of the photoanode $Ti/Fe_2O_3/Cu_2S/Co(OH)_x$ [Figure 2G] was carried out. The results [Figure 2H-L] show that $Ti/Fe_2O_3/Cu_2S/Co(OH)_x$ nanorods contain both Fe, O, Cu, S, and Co, and all five elements are relatively uniformly distributed on the nanorods.

Figure 3A shows the XRD results of three types of photoanodes. By comparing them with standard cards (PDF#44-1294) and (PDF#33-0664), it is proven that they are the characteristic XRD peaks of metal Ti and Fe_2O_3. The XRD results showed that the structure of Fe_2O_3 remained unchanged during the preparation and electrochemical deposition of SILAR. At the same time, no XRD peaks of Cu_2S and $Co(OH)_x$ were observed, indicating a relatively low content of Cu_2S and $Co(OH)_x$. Additionally, the XRD fine maps of these three photoanodes from 32.5° to 34.0° [Figure 3B] reflected that the introduction of a small amount of Cu_2S and $Co(OH)_x$ did not shift the X-ray characteristic diffraction peaks of Fe_2O_3 and metal Ti, which indicated that Cu_2S and $Co(OH)_x$ did not alter the physical phases of Fe_2O_3 and metal Ti. They were only loaded or encapsulated on the Fe_2O_3 and metal Ti.

Surface analysis and elemental composition

XPS was performed on Ti/Fe_2O_3, $Ti/Fe_2O_3/Cu_2S$, and $Ti/Fe_2O_3/Cu_2S/Co(OH)_x$ photoanodes to confirm the formation of heterostructures and analyze the chemical states of elements. The XPS full spectrum [Figure 4A] reveals that the $Ti/Fe_2O_3/Cu_2S/Co(OH)_x$ photoanode comprises Fe, O, Cu, S, and Co. Similarly, the other two photoanodes also exhibit the presence of these elements. In the Fe 2p region [Figure 4B], the XPS spectra reveal two peaks at approximately 724 and 711 eV, characteristic of Fe^{3+}, along with two satellite peaks observed at 732.74 and 718.35 eV. It can be seen from the figure that the two main peaks at about 724 and 711 eV confirm the presence of Fe^{3+} as the main component on these three photoanodes; these main peaks are also accompanied by satellite peaks at about 733 and 718 eV, also indicative of Fe^{3+} presence; the XPS peaks of these three photoanodes show no shifts[32,33]. As can be seen from Figure 4C, the peak of the Fe–O bond of these three samples is around 529.8 eV without a significant shift. Compared to Ti/Fe_2O_3, the peaks corresponding to the high binding energy of the O element in $Ti/Fe_2O_3/Cu_2S$ and $Ti/Fe_2O_3/Cu_2S/Co(OH)_x$ are shifted towards higher binding energies, attributed to the formation of S–O bonds[20]. In the Cu 2p spectrum [Figure 4D], the peaks observed at 951.90 and 932.03 eV correspond well to Cu $2p^{1/2}$ and Cu $2p^{3/2}$ of Cu^+. Additionally, the absence of the characteristic jitter peak between the Cu $2p^{1/2}$ and $2p^{3/2}$ peaks suggests the absence of Cu^{2+}[34,35]. Consistent with the findings in the Cu 2p spectrum, the presence of two peaks at S $2p^{1/2}$ (163.4 eV) and S $2p^{3/2}$ (162.3 eV) [Figure 4E] confirms the formation of Cu_2S[20]. Compared with Ti/Fe_2O_3, a pair of weak peaks were observed at 164.3 and 162.3 eV for the as-prepared $Ti/Fe_2O_3/Cu_2S$ and $Ti/Fe_2O_3/Cu_2S/Co(OH)_x$ photoanodes, which were assigned to Cu_2S. The S–O bond between Fe_2O_3 is completely consistent with previous reports[36,37]. The Co 2p spectrum [Figure 4F] also shows two main peaks near 781 eV (corresponding to Co $2p^{3/2}$), and a dithered satellite peak (near 786 eV), which corresponds to Co^{3+} and Co^{2+}, respectively[38,39]. The fitting results show that the content of Co^{3+} in the composite is relatively higher than that of Co^{2+}, which is beneficial for obtaining excellent catalytic activity[38]. In addition, a satellite peak located near 786 eV can be attributed to the Co hydroxyl group[40]. The formation of Co hydroxyl groups will have a positive impact on the OER performance, as it may induce structural flexibility and an optimized coordination state[41].

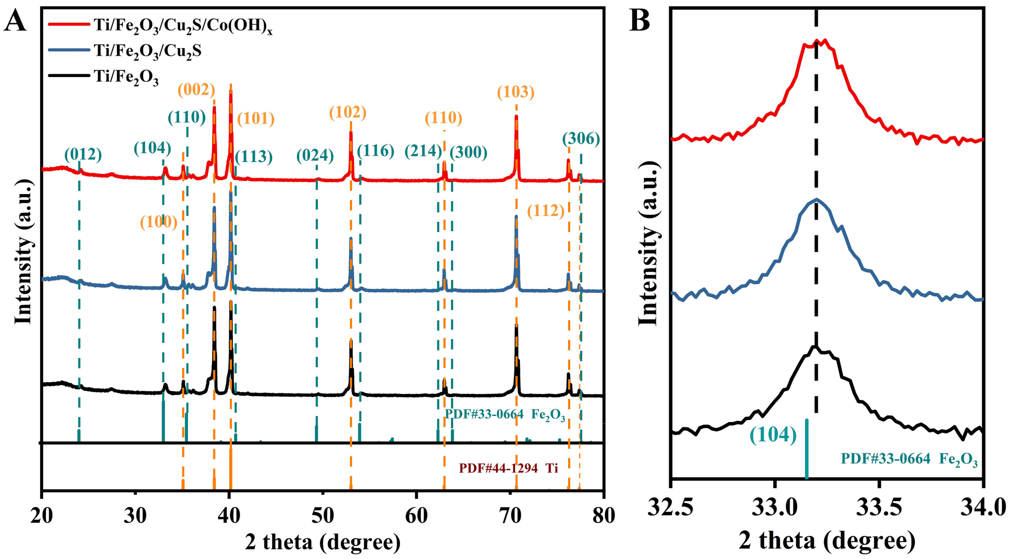

Figure 3. (A) XRD patterns of Ti/Fe_2O_3, Ti/Fe_2O_3/Cu_2S, and Ti/Fe_2O_3/Cu_2S/$Co(OH)_x$ photoanodes; (B) XRD fine patterns of Ti/Fe_2O_3, Ti/Fe_2O_3/Cu_2S, and Ti/Fe_2O_3/Cu_2S/$Co(OH)_x$ photoanodes. XRD: X-ray diffraction.

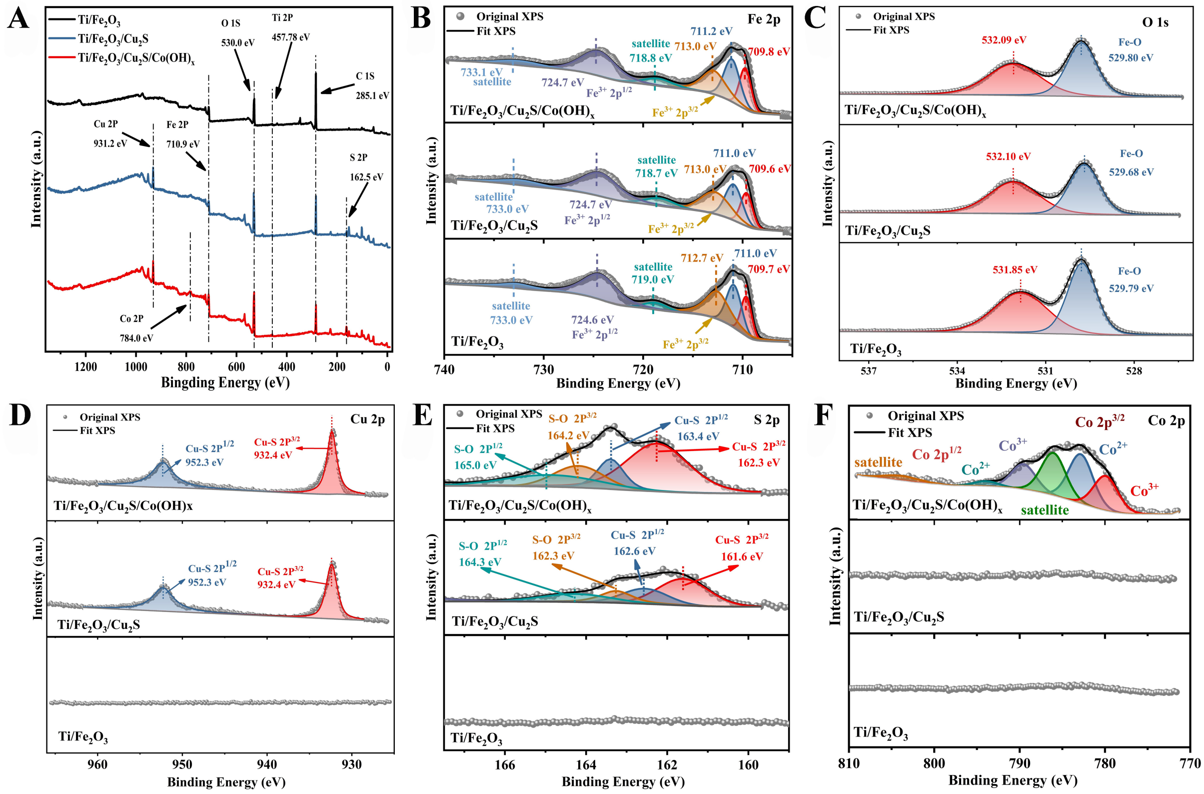

Figure 4. XPS spectra of Ti/Fe_2O_3, Ti/Fe_2O_3/Cu_2S, and Ti/Fe_2O_3/Cu_2S/$Co(OH)_x$ photoanodes. (A) the survey spectra; (B) Fe 2p; (C) O 1s; (D) Cu 2p; (E) S 2p; and (F) Co 2p. XPS: X-ray photoelectron spectroscopy.

As shown in Figure 5A, the trend of the curves of the UV-vis absorption spectra of these three photoanodes is consistent, and the test results illustrate that the absorption of these three samples is relatively strong in

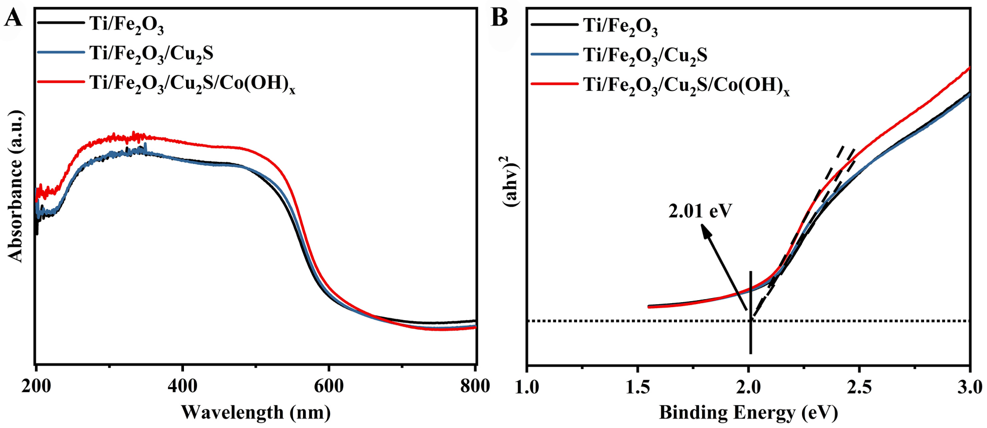

Figure 5. (A) UV-Vis absorption spectra of Ti/Fe$_2$O$_3$, Ti/Fe$_2$O$_3$/Cu$_2$S, and Ti/Fe$_2$O$_3$/Cu$_2$S/Co(OH)$_x$ photoanodes; (B) The bandgap diagram of Ti/Fe$_2$O$_3$, Ti/Fe$_2$O$_3$/Cu$_2$S, and Ti/Fe$_2$O$_3$/Cu$_2$S/Co(OH)$_x$ photoanodes. UV-Vis: Ultraviolet-visible.

the UV region and in the visible region from 420 to 600 nm. The bandgap can be estimated from the Tauc plot [Equation (1)][42], so that the bandgap of Fe$_2$O$_3$, the main semiconductor material of the three photoanodes, can be deduced from the test results of the UV-Vis diffuse reflectance spectra to be 1.98 eV [Figure 5B].

PEC and EC analysis

PEC measurement

A series of PEC tests[43] were used to characterize the iron oxide nanorod photoanode[44]. The LSV results [Figure 6A] indicate the photocurrent performance of different samples in a 1 M KOH electrolyte solution at potentials ranging from 0.7 (*vs.* RHE) to 1.6 V (*vs.* RHE). Under AM 1.5G irradiation, as P-type Cu$_2$S semiconductors and ultra-thin Co(OH)$_x$ nanosheets were gradually introduced, the photocurrent density of the photoanode significantly increased. The Ti/Fe$_2$O$_3$/Cu$_2$S/Co(OH)$_x$ photoanode showed the highest photocurrent density, about 4.81 mA/cm^2 at 1.23 V (*vs.* RHE), which was about three times that of the original Ti/Fe$_2$O$_3$ (1.62 mA/cm^2). Under visible light irradiation (Figure 6B, λ > 420 nm, 66.7 mW/cm^2), the photocurrent density of the Ti/Fe$_2$O$_3$/Cu$_2$S/Co(OH)$_x$ photoanode is about half of that under AM 1.5G irradiation, measuring about 2.39 mA/cm^2 at 1.23 V (*vs.* RHE). This indicates good visible photocatalytic activity. We also explored the advantages of one-dimensional morphology in observing high photocurrents [Supplementary Figure 2]. In addition, different Cu$_2$S and Co(OH)$_x$ contents affect the PEC characteristics of Ti/Fe$_2$O$_3$ [Supplementary Figure 3].

Supplementary Table 1 shows the PEC performance of the Ti/Fe$_2$O$_3$/Cu$_2$S/Co(OH)$_x$ photoanodes in this study compared to other recently reported Fe$_2$O$_3$-based photoanodes. The final comparison results show the excellent performance of our prepared photoanode.

The ABPE [Figure 6C] of each photoanode below the water oxidation thermodynamic potential (1.23 V *vs.* RHE) was calculated based on the LSV results[45]. Figure 6C illustrates that the ABPE efficiency of the Ti/Fe$_2$O$_3$/Cu$_2$S/Co(OH)$_x$ photoanode was significantly enhanced compared with Ti/Fe$_2$O$_3$, Ti/Fe$_2$O$_3$/Cu$_2$S, and Ti/Fe$_2$O$_3$/Co(OH)$_x$. At 1.03 V (*vs.* RHE), it reached 0.48%, which is 3.2 times higher than that of the Ti/Fe$_2$O$_3$ photoanode (0.15%, 1.03 V *vs.* RHE). Furthermore, under visible light irradiation (λ > 420 nm, light intensity 66.7 mW/cm^2, Figure 6D), the Ti/Fe$_2$O$_3$/Cu$_2$S/Co(OH)$_x$ photoanode exhibited the highest ABPE of 0.2%.

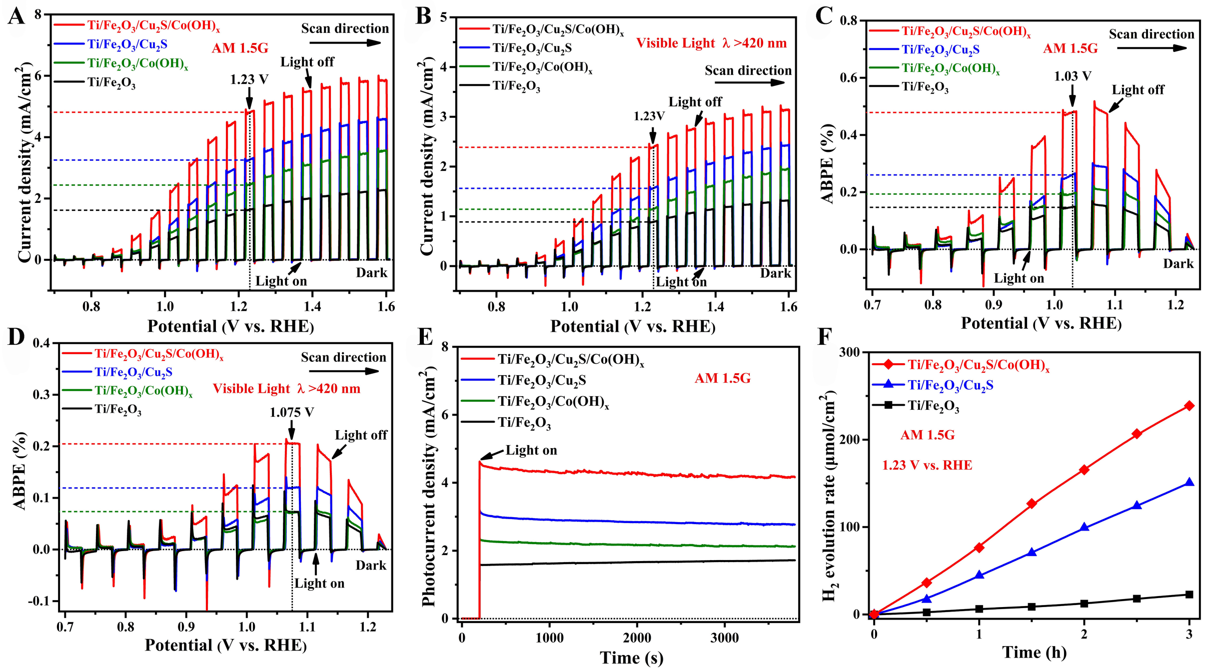

Figure 6. PEC performance of Ti/Fe_2O_3, $Ti/Fe_2O_3/Cu_2S$, and $Ti/Fe_2O_3/Cu_2S/Co(OH)_x$ photoanodes. (A) Chopped LSV curves under AM 1.5G (100 mW/cm^2); (B) Chopped LSV curves under visible light (λ > 420 nm, 66.7 mW/cm^2); (C) ABPE curves under AM 1.5G (100 mW/cm^2); (D) ABPE curves under visible light irradiation (λ > 420 nm, 66.7 mW/cm^2); (E) I-t data plots at 1.23 V *vs.* RHE; (F) PEC H_2 evolution across different samples at 1.23 V *vs.* RHE. PEC: Photoelectrochemical; LSV: linear sweep voltammetry; ABPE: applied bias photon-to-current efficiency; RHE: reversible hydrogen electrode.

I-t and measurement of light-assisted H_2 production

To verify the stability of the prepared photoanode, chronoamperometry (I-t) was conducted [Figure 6E]. Under continuous illumination for 1 h, the $Ti/Fe_2O_3/Cu_2S/Co(OH)_x$ (I-t, 1.23 V *vs.* RHE) photoanode showed good stability, and the photocurrent remained almost unchanged. To further demonstrate the stability of the synthesized samples, a 19-hour stability test [Supplementary Figure 4] was performed on top of the original 1-hour test [Figure 6E]. The results indicated that the samples exhibited enhanced stability. Following the stability tests, the samples were subjected to a series of characterizations [Supplementary Figures 5-11].

The actual H_2 generation performance of various samples at 1.23 V (*vs.* RHE) was recorded to investigate the relevance of the observation of photocurrent to the solar-assisted hydrolysis H_2 generation reaction. Photoanodes with high photocurrent density often exhibit higher hydrogen production rates under optoelectronic conditions. The 3-hour measurement period [Figure 6F] showed a linear increase in the amount of H_2 generation over time, indicating a stable H_2 generation rate for the sample and reaffirming the stability of the $Ti/Fe_2O_3/Cu_2S/Co(OH)_x$ photoanode.

IPCE measurement

In order to explore the response of the photoanode to different wavelengths of light, the prepared photoanode was used to conduct the IPCE test. During the test, the light source irradiates from 300 nm, changes to 600 nm at a constant speed, and ends at 600 nm; the wavelength resolution of the spectral analysis is 1 nm. It can be seen from Figure 7A that under the electrochemical noise mode, the pristine Ti/Fe_2O_3 photoanode has photocurrent performance in the wavelength region of 300-600 nm, which indicates that Fe_2O_3 material has a wide light absorption range and an excellent visible light response.

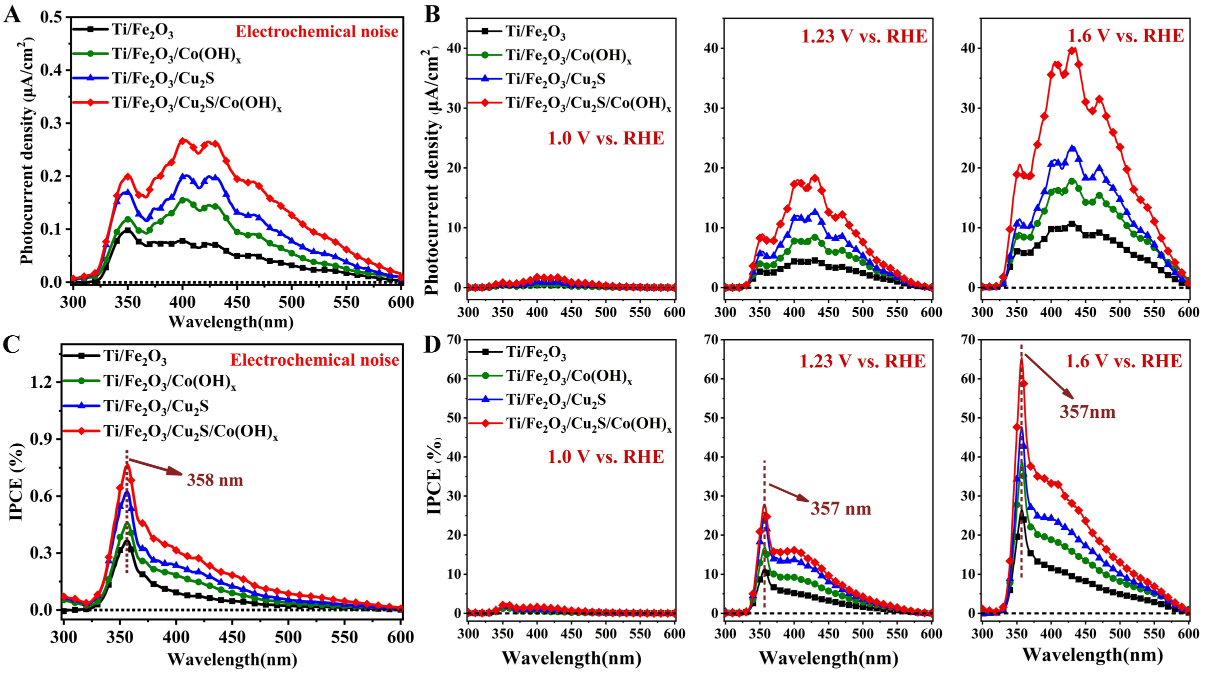

Figure 7. (A and B) Photocurrent density *vs.* the monochromatic light; (C and D) Derived IPCE (%) spectra of samples under different bias. IPCE: Incident monochromatic photon electron conversion efficiency.

Compared with Ti/Fe_2O_3, the photocurrent densities and IPCE values of Ti/Fe_2O_3/Cu_2S, Ti/Fe_2O_3/Co$(OH)_x$, and Ti/Fe_2O_3/Cu_2S/Co$(OH)_x$ photoanodes gradually increase, which shows that the introduction of Cu_2S and Co$(OH)_x$ improves the photoelectric performance of Fe_2O_3; this improvement covers the entire wavelength range from 300 to 600 nm. Under the constant potential polarization mode with different applied bias voltages [Figure 7B], the photocurrent density and IPCE value of these photoanodes gradually increase with higher bias voltages, which shows that increasing the applied bias voltage is helpful for photogenerated current carrying. The separation of electrons strengthens the photoelectric properties of the sample. Under the conditions of the electrochemical noise test [Figure 7C] and constant potential test [Figure 7D], the IPCE peaks of Ti/Fe_2O_3, Ti/Fe_2O_3/Cu_2S, Ti/Fe_2O_3/Co$(OH)_x$, and Ti/Fe_2O_3/Cu_2S/Co$(OH)_x$ photoanodes are all at 357 nm place. Under electrochemical noise test conditions, at 1.23 (*vs.* RHE) and 1.6 V (*vs.* RHE), the peak IPCE values of the Ti/Fe_2O_3/Cu_2S/Co$(OH)_x$ photoanode are 0.76%, 27.6%, and 64.7%, respectively.

MS analysis

To investigate the energy band structure information of the Ti/Fe_2O_3/Cu_2S/Co$(OH)_x$ photoanode, key parameters such as the conduction band (CB), flat band potential, and carrier concentration were determined. The effects of the introduction of Cu_2S and Co$(OH)_x$ on the Ti/Fe_2O_3 photoanode were also examined. Therefore, Ti/Fe_2O_3, Ti/Fe_2O_3/Cu_2S, Ti/Fe_2O_3/Co$(OH)_x$ and Ti/Fe_2O_3/Cu_2S/Co$(OH)_x$ photoanodes were all subjected to MS tests.

The longest segment of the MS curve makes an extension line to get the intersection with the baseline for the flat-charged potential position. The intersection of the extension lines for the different frequencies of the four photoanodes is a single point[46]. The positive slopes of the tangent lines for all four samples indicate their n-type nature[20]. In both n- and p-type semiconductors, the flat band potential can be approximated as the CB potential. The results shown in Figure 8A-D indicate that the introduction of both Cu_2S and

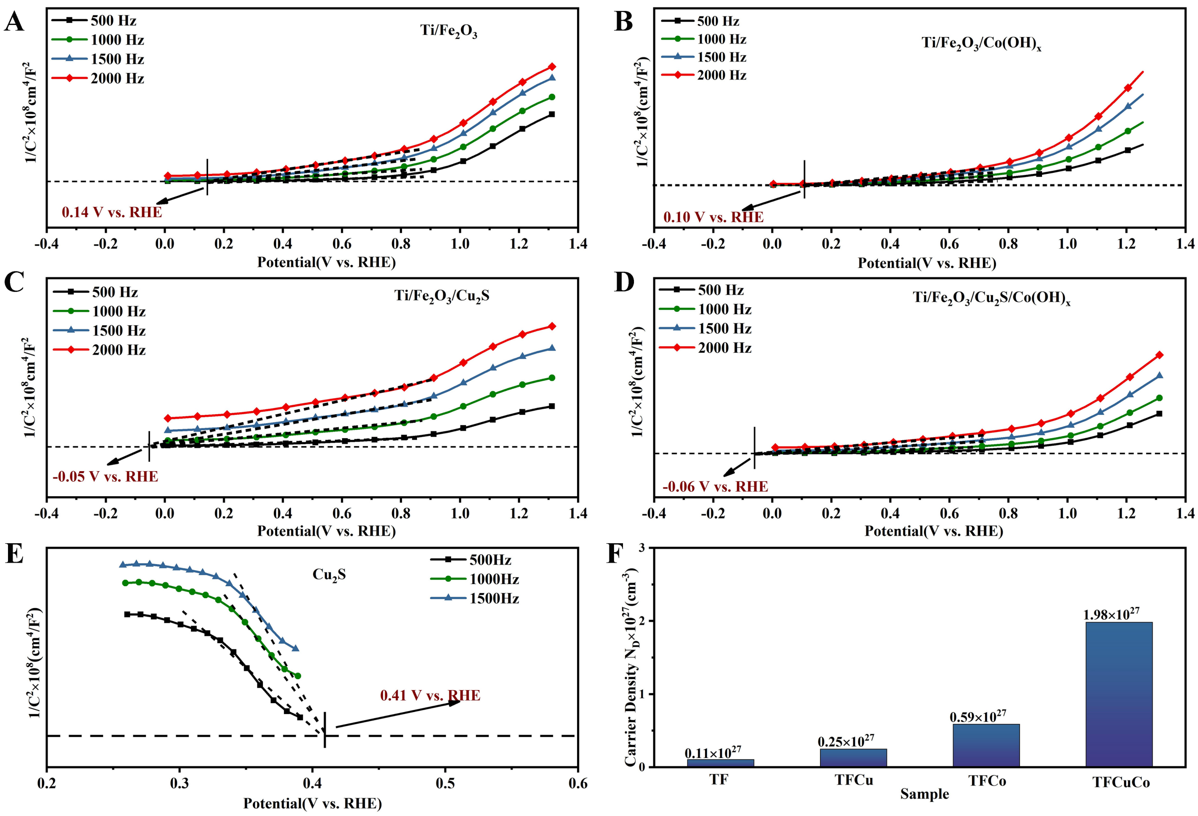

Figure 8. Mott-Schottky plots have frequencies from 500 to 2,000 Hz. (A) Ti/Fe_2O_3 photoanode; (B) $Ti/Fe_2O_3/Cu_2S$ photoanode; (C) $Ti/Fe_2O_3/Co(OH)_x$ photoanode; (D) $Ti/Fe_2O_3/Cu_2S/Co(OH)_x$ photoanode; (E) Frequency (500 to 1,500 Hz) of the Mott-Schottky diagram of Cu_2S nanoparticles; (F) The carrier concentrations of Ti/Fe_2O_3 photoanode (TF), $Ti/Fe_2O_3/Cu_2S$ photoanode (TFCu), $Ti/Fe_2O_3/Co(OH)_x$ photoanode (TFCo), and $Ti/Fe_2O_3/Cu_2S/Co(OH)_x$ photoanode (TFCuCo).

$Co(OH)_x$ results in a more negative flat-band potential for the Ti/Fe_2O_3 photoanode. Compared to the Ti/Fe_2O_3 photoanode, the CB potential of the $Ti/Fe_2O_3/Co(OH)_x$, $Ti/Fe_2O_3/Cu_2S$, and $Ti/Fe_2O_3/Cu_2S/Co(OH)_x$ photoanodes were reduced from 0.14 (*vs.* RHE for Ti/Fe_2O_3) to 0.10, -0.05, and -0.06 V (*vs.* RHE), respectively. A negative movement of the flat band potential suggests a reduced energy potential barrier for electron transfer at the interface, contributing to a reduction in the charge transfer resistance[44]. Therefore, compared with the other three, the $Ti/Fe_2O_3/Cu_2S/Co(OH)_x$ photoanode has the most negative CB potential and the best photocurrent and photocoupling hydrogen production performance, corresponding to the previous results.

Separately synthesized Cu_2S powders were also tested for MS; the results are shown in Figure 8E. The intersection of the extension lines of the data curves for the three different frequencies is a point whose tangent line has a negative slope, which reveals that the Cu_2S semiconductor has p-type properties[47] with a flat-band potential (approximated as the conduction-band potential) of 0.14 V (*vs.* RHE). The carrier concentrations of these four photoanodes were calculated from the MS test data [Figure 8F]. The results show that the carrier concentration of the $Ti/Fe_2O_3/Cu_2S/Co(OH)_x$ photoanode is one magnitude higher compared with that of the Ti/Fe_2O_3, $Ti/Fe_2O_3/Cu_2S$, and $Ti/Fe_2O_3/Co(OH)_x$, which is one of the reasons for its good performance.

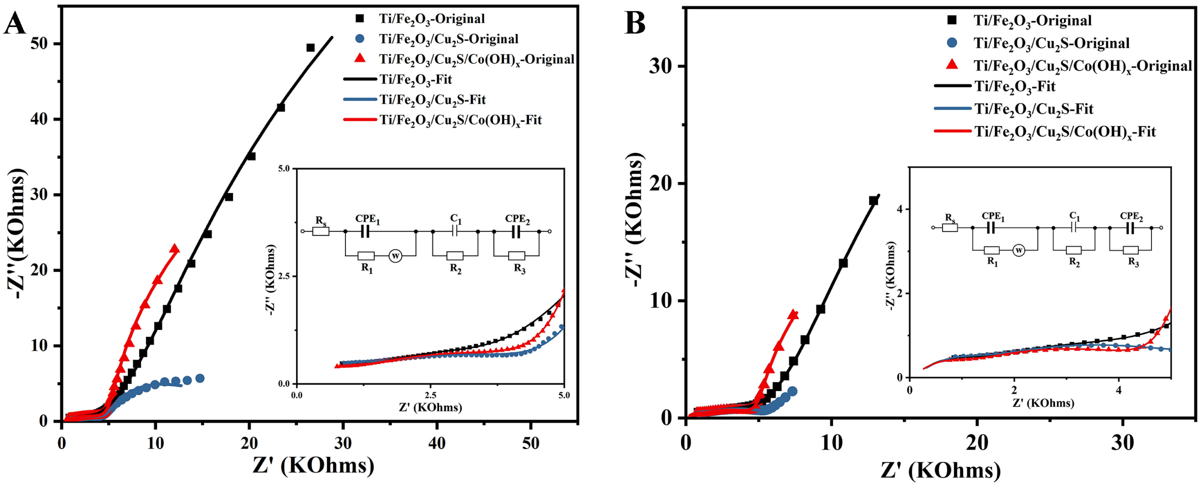

Figure 9. EIS and Equivalent Circuit of Ti/Fe_2O_3 photoanode, Ti/Fe_2O_3/Cu_2S photoanode and Ti/Fe_2O_3/Cu_2S/$Co(OH)_x$ photoanode at (A) 1.23 V *vs.* RHE and at (B) OCP. EIS: Electrochemical impedance spectroscopy; RHE: reversible hydrogen electrode; OCP: open circuit potential.

EIS analysis

Frequency transmission characteristics and electrochemical properties of photoanodes were studied using EIS[48]. Nyquist plots were obtained for the samples under dark conditions at open-circuit potential [Figure 9A] and at 1.23 V (*vs.* RHE) [Figure 9B]. Measurements were conducted in the frequency range of 100 MHz to 100 kHz. The equivalent circuit [Figure 9] includes a resistor (R), a capacitor (C), a constant phase element (CPE), and a Warburg impedance element (W). From the small figure in Figure 9A, it can be seen (under open-circuit potential conditions) that the radii of the arcs of the EIS curves are smaller than those of Ti/Fe_2O_3/Cu_2S and Ti/Fe_2O_3/Cu_2S/$Co(OH)_x$ in the high-frequency region (0-5 KOhms); moreover, from the internal small figure in Figure 9B, it can be seen that the radii of the arcs of the EIS curves are smaller than those of Ti/Fe_2O_3 and Ti/Fe_2O_3/Cu_2S/$Co(OH)_x$ in the high-frequency region (0-5 KOhms). Specifically, the arc radius of the EIS curve for Ti/Fe_2O_3/Cu_2S/$Co(OH)_x$ is smaller than that of both Ti/Fe_2O_3 and Ti/Fe_2O_3/Cu_2S. A lower arc radius means a lower charge transfer resistance in the electrode, facilitating rapid separation and transfer of photogenerated carriers[49]. The fitted data for the curves measured at 1.23 V (*vs.* RHE) are presented in Supplementary Table 2, and these values are significantly lower for Ti/Fe_2O_3/Cu_2S and Ti/Fe_2O_3/Cu_2S/$Co(OH)_x$ compared with R_s, R_2, R_3, and Z_w for Ti/Fe_2O_3, which are also in the same order of magnitude with little difference in R_1[44]. The capacitance of the electrode bilayers C_1 and CPE_2 is also improved significantly, and these three CPE_1 are also in the same order of magnitude with little difference. The value of R_2 decreases significantly from 140 KΩ for Ti/Fe_2O_3 to 6.07 KΩ for Ti/Fe_2O_3/Cu_2S, and R_3 reduces from 1,220 Ω for Ti/Fe_2O_3 to 509 Ω for Ti/Fe_2O_3/Cu_2S/$Co(OH)_x$ of 509 Ω. In addition, the fitted data for the curves measured at open-circuit potentials [Supplementary Table 3] reflect the same trend. These results indicate that introducing P-type Cu_2S nanoparticle semiconductors and electrodeposition of an ultrathin layer of $Co(OH)_x$ improved the charge transport of iron oxide and promoted the surface photogenerated carrier separation and transfer. $\eta_{surface}$ curves prove it even further [Supplementary Figure 12].

Mechanistic analysis and bandgap calculation

The E_g of the photoanode samples are calculated using Tauc plots, which depict [(IPCE% × hv)$^{1/2}$ against photon energy (hv)] in the electrochemical noise mode[44] [Figure 10A]. The main component of all four photoanodes is α-Fe_2O_3, so they all reflect the E_g of α-Fe_2O_3 of 2.10 eV, which agrees with the previously reported results[50]. The E_g can be evaluated from the Tauc plot [Equation (1)]. The E_g [Figure 10B] of the

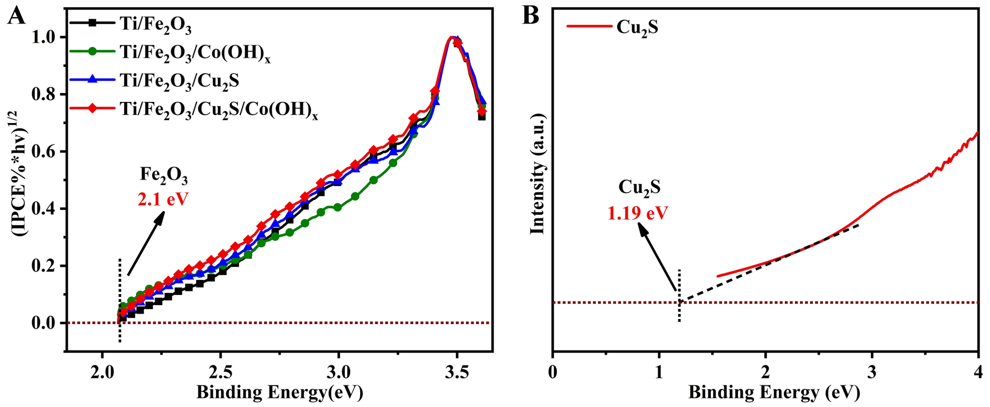

Figure 10. (A) The bandgap energy (E_g) Ti/Fe_2O_3 photoanode, Ti/Fe_2O_3/Cu_2S photoanode, Ti/Fe_2O_3/ $Co(OH)_x$ photoanode and Ti/Fe_2O_3/Cu_2S/$Co(OH)_x$ photoanode calculated through IPCE testing; (B) The bandgap energy (E_g) of Cu_2S nanoparticles calculated through UV-vis-DRS testing. IPCE: incident monochromatic photon electron conversion efficiency; UV-vis-DRS: ultraviolet-visible diffuse reflectance spectroscopy.

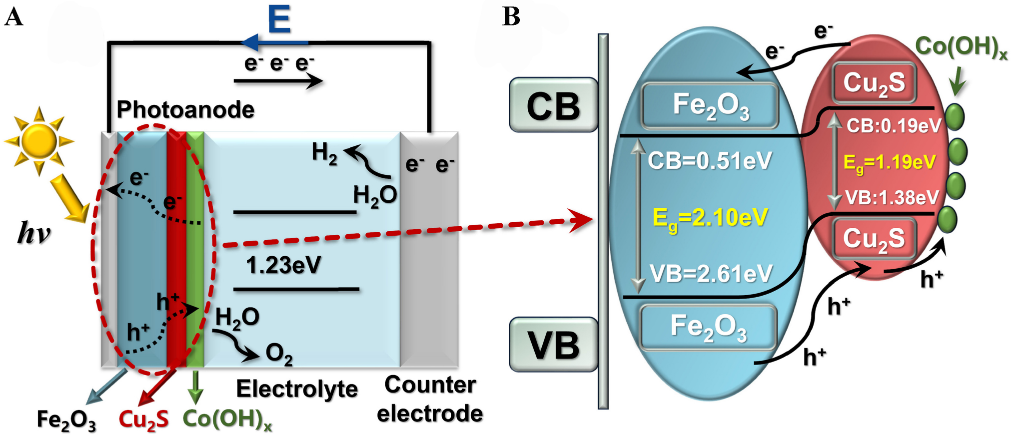

Figure 11. (A) Photoanode Ti/Fe_2O_3/Cu_2S/$Co(OH)_x$ photoelectric hydrogen production mechanism diagram; (B) Photoanode Ti/Fe_2O_3/Cu_2S/$Co(OH)_x$ energy band gap diagram.

Cu_2S semiconductor nanoparticles alone was calculated by UV-vis spectroscopy test as 1.19 eV.

Figure 11A and B shows the E_g structure map based on the IPCE electrochemical noise pattern, UV-vis spectroscopy, and MS measurements. The valence band (VB) of the photocatalytic sample is determined from the estimated CB and E_g. Results indicate that the VB and CB of n-Fe_2O_3 are 2.24 and 0.14 V, respectively, while those of p-Cu_2S are 0.41 and 0.14 V, respectively.

By the observations of the above experiments, we present the charge separation mechanism of ultra-thin $Co(OH)_x$ package p-Cu_2S/n-Fe_2O_3 to explain its strengthened PEC properties [Figure 9][19,51]. Before contact, the CB and VB energy levels of p-type Cu_2S are higher than those of n-type Fe_2O_3, whereas the Fermi energy level (EF) of Cu_2S is lower than that of Fe_2O_3. After forming the p-n junction heterostructure, the energy level of Cu_2S rises while that of Fe_2O_3 decreases, leading to an equilibrium of their EFs. Consequently, an internal electric field is formed at the Fe_2O_3/Cu_2S interface under thermodynamic equilibrium conditions. Due to the energy matching between Fe_2O_3 and Cu_2S, their energy bands shift together until the Fermi levels align, resulting in band bending in the space charge region. Electrons generated and separated in the CB of

Cu_2S move to the CB of Fe_2O_3, while holes separated and retained in the VB of Fe_2O_3 flow to the VB of Cu_2S to react with the electrolyte. Therefore, the p-Cu_2S/n-Fe_2O_3 heterojunction photoanode enhances photogenerated electron-hole pair separation and improves light harvesting efficiency. After modification with the $Co(OH)_x$ co-catalyst on Fe_2O_3/Cu_2S, photogenerated electrons are efficiently transferred from Fe_2O_3/Cu_2S to the Pt electrode with high electron mobility. Meanwhile, holes migrating to the surface or subsurface are captured by the outermost $Co(OH)_x$ catalyst and react with the electrolyte, increasing hole mobility and optimizing the kinetics of hole-mediated water oxidation.

CONCLUSIONS

In conclusion, we synthesized an ultrathin $Co(OH)_x$-encapsulated p-Cu_2S/n-Fe_2O_3, which enhances charge separation and surface oxygen evolution kinetics of the iron oxide nanorod array photoanode through the synergistic effect of p-n heterojunctions and OECs. In 1 M KOH solution [25 °C, AM 1.5G, 1.23 V (*vs.* RHE)], the photocurrent density of $Ti/Fe_2O_3/Cu_2S/Co(OH)_x$ is about three times that of Ti/Fe_2O_3, reaching 4.8 mA/cm^2. Under visible light irradiation [$\lambda > 420$ nm, AM 1.5G, 1.23 V (*vs.* RHE)], its photocurrent density also reaches 2.4 mA/cm^2, which is half of the full spectrum light; in addition, the corresponding optical response limit is extended to 600 nm. Without sacrificial agents and photosensitizers, we observed a significant increase in the hydrogen evolution rate of $Ti/Fe_2O_3/Cu_2S/Co(OH)_x$, reaching 76.4 $\mu mol/cm^2$. Our work provides a novel concept for photoanode PEC water splitting.

DECLARATIONS

Authors' contributions

Prepared and revised the manuscript: Shi HY, Ji MH, Zhou QQ, Li KX, Wang HL, Chen R
Designed and revised the manuscript: Chen YX, Lin XM, Lu CZ
All authors contributed to the discussion and preparation of the manuscript.

Availability of data and materials

The authors confirm that the data supporting the findings of this study are available within its Supplementary Materials.

Financial support and sponsorship

Authors are thankful for the financial support of the Natural Science Foundation of Fujian Province (2023H0046), the XMIREM autonomously deployment project (2023CX10, 2023GG01), the National Natural Science Foundation of China (22275185), the Major Research Project of Xiamen (3502Z20191015), and the Fujian Science & Technology Innovation Laboratory for Optoelectronic Information of China (2021ZR132, 2021ZZ115).

Conflicts of interest

Chen YX is the Junior Editorial Board Member of *Chemical Synthesis*, while the other authors have declared that they have no conflicts of interest.

Ethical approval and consent to participate

Not applicable.

Consent for publication

Not applicable.

Copyright

REFERENCES

1. Bie C, Wang L, Yu J. Challenges for photocatalytic overall water splitting. *Chem* 2022;8:1567-74. DOI
2. Wang Z, Gu Y, Zheng L, et al. Machine learning guided dopant selection for metal oxide-based photoelectrochemical water splitting: the case study of Fe_2O_3 and CuO. *Adv Mater* 2022;34:e2106776. DOI PubMed
3. Liu B, Wang S, Zhang G, et al. Tandem cells for unbiased photoelectrochemical water splitting. *Chem Soc Rev* 2023;52:4644-71. DOI PubMed
4. Li Y, Zhang D, Qiao W, et al. Nanostructured heterogeneous photocatalyst materials for green synthesis of valuable chemicals. *Chem Synth* 2022;2:9. DOI
5. Fujishima A, Honda K. Electrochemical photolysis of water at a semiconductor electrode. *Nature* 1972;238:37-8. DOI PubMed
6. Nayak AK, Sohn Y, Pradhan D. Facile green synthesis of $WO_3{\cdot}H_2O$ nanoplates and WO_3 nanowires with enhanced photoelectrochemical performance. *Cryst Growth Des* 2017;17:4949-57. DOI
7. Zhao HP, Zhu ML, Shi HY, et al. Cerium-doped iron oxide nanorod arrays for photoelectrochemical water splitting. *Molecules* 2022;27:9050. DOI PubMed PMC
8. Li C, Luo Z, Wang T, Gong J. Surface, bulk, and interface: rational design of hematite architecture toward efficient photoelectrochemical water splitting. *Adv Mater* 2018;30:e1707502. DOI PubMed
9. Tang P, Arbiol J. Engineering surface states of hematite based photoanodes for boosting photoelectrochemical water splitting. *Nanoscale Horiz* 2019;4:1256-76. DOI
10. Gao L, Chai H, Niu H, Jin J, Ma J. Roles of cobalt-coordinated polymeric perylene diimide in hematite photoanodes for improved water oxidation. *Small* 2023;19:e2302665. DOI PubMed
11. Wu J, Cheng Y, Lin J, Huang Y, Huang M, Hao S. Fabrication and photocatalytic properties of $HLaNb_2O_7$/(Pt, Fe_2O_3) pillared nanomaterial. *J Phys Chem C* 2007;111:3624-8. DOI
12. Wang H, Hu Y, Song G, Zheng D. Intrinsic and extrinsic doping to construct hematite nanorod p-n homojunctions for highly efficient PEC water splitting. *Chem Eng J* 2022;435:135016. DOI
13. Fujimoto H, Nakayasu B, Tobisu M. Synthesis of γ-lactams from acrylamides by single-carbon atom doping annulation. *J Am Chem Soc* 2023;145:19518-22. DOI PubMed
14. Li F, Yue X, Liao Y, Qiao L, Lv K, Xiang Q. Understanding the unique S-scheme charge migration in triazine/heptazine crystalline carbon nitride homojunction. *Nat Commun* 2023;14:3901. DOI PubMed PMC
15. Zhang M, Mao Y, Bao X, et al. Coupling benzylamine oxidation with CO_2 photoconversion to ethanol over a black phosphorus and bismuth tungstate S-scheme heterojunction. *Angew Chem Int Ed Engl* 2023;62:e202302919. DOI PubMed
16. Shen H, Qu F, Xia Y, Jiang X. Straightforward and ultrastable surface modification of microfluidic chips with norepinephrine bitartrate improves performance in immunoassays. *Anal Chem* 2018;90:3697-702. DOI PubMed
17. Li Z, Zhang Z. Tetrafunctional Cu_2S thin layers on Cu_2O nanowires for efficient photoelectrochemical water splitting. *Nano Res* 2018;11:1530-40. DOI
18. Guo K, Liu Z, Zhou C, et al. Fabrication of TiO_2 nano-branched arrays/Cu_2S composite structure and its photoelectric performance. *Appl Catal B Environ* 2014;154-5:27-35. DOI
19. He B, Wang Y, Liu X, et al. Spatial engineering of a $Co(OH)_x$ encapsulated p-Cu_2S/n-$BiVO_4$ photoanode: simultaneously promoting charge separation and surface reaction kinetics in solar water splitting. *J Mater Chem A* 2019;7:6747-52. DOI
20. Zhang Y, Huang Y, Zhu SS, et al. Covalent S–O bonding enables enhanced photoelectrochemical performance of Cu_2S/Fe_2O_3 heterojunction for water splitting. *Small* 2021;17:e2100320. DOI PubMed
21. Wu Y, Yao S, Lv G, et al. Construction of p-n junctions in single-unit-cell $ZnIn_2S_4$ nanosheet arrays toward promoted photoelectrochemical performance. *J Catal* 2021;401:262-70. DOI
22. Li Z, Li J, Wang W, et al. Near zero-threshold voltage P-N junction diodes based on super-semiconducting nanostructured Ag/Al arrays. *Adv Mater* 2023;35:e2210612. DOI PubMed
23. Zhao Y, Westerik P, Santbergen R, Zoethout E, Gardeniers H, Bieberle-hütter A. From geometry to activity: a quantitative analysis of WO_3/Si micropillar arrays for photoelectrochemical water splitting. *Adv Funct Mater* 2020;30:1909157. DOI
24. Meng L, Zhou X, Wang S, et al. A plasma-triggered O-S bond and P-N junction near the surface of a SnS_2 nanosheet array to enable efficient solar water oxidation. *Angew Chem Int Ed Engl* 2019;58:16668-75. DOI PubMed
25. Wu Y, Liu X, Zhang H, et al. Atomic sandwiched p-n homojunctions. *Angew Chem Int Ed Engl* 2021;60:3487-92. DOI PubMed
26. Mcdonald KJ, Choi KS. Photodeposition of Co-based oxygen evolution catalysts on α-Fe_2O_3 photoanodes. *Chem Mater* 2011;23:1686-93. DOI
27. Yang G, Li Y, Pang H, Chang K, Ye J. Ultrathin cobalt–manganese nanosheets: an efficient platform for enhanced photoelectrochemical water oxidation with electron-donating effect. *Adv Funct Mater* 2019;29:1904622. DOI
28. Yang Z, Jiang Y, Zhang W, et al. Solid-state, low-cost, and green synthesis and robust photochemical hydrogen evolution performance of ternary $TiO_2/MgTiO_3$/C photocatalysts. *iScience* 2019;14:15-26. DOI PubMed PMC
29. An Y, Lin C, Dong C, et al. Scalable photoelectrochemical cell for overall solar water splitting into H_2 and H_2O_2. *ACS Energy Lett*

2024;9:1415-22. DOI

30. Cao Q, Che R, Chen N. Scalable synthesis of Cu_2S double-superlattice nanoparticle systems with enhanced UV/visible-light-driven photocatalytic activity. *Appl Catal B Environ* 2015;162:187-95. DOI
31. Li J, Li J, Yuan H, Zhang W, Jiao Z, Song Zhao X. Modification of $BiVO_4$ with partially covered α-Fe_2O_3 spindles serving as hole-transport channels for significantly improved photoelectrochemical performance. *Chem Eng J* 2020;398:125662. DOI
32. Yi S, Wulan B, Yan J, Jiang Q. Highly efficient photoelectrochemical water splitting: surface modification of cobalt-phosphate-loaded Co_3O_4/Fe_2O_3 p–n heterojunction nanorod arrays. *Adv Funct Mater* 2019;29:1801902. DOI
33. Gota S, Guiot E, Henriot M, Gautier-soyer M. Atomic-oxygen-assisted MBE growth of α-Fe_2O_3 on α-Al_2O_3 (0001): metastable FeO(111)-like phase at subnanometer thicknesses. *Phys Rev B* 1999;60:14387-95. DOI
34. Liu P, Hensen EJ. Highly efficient and robust Au/$MgCuCr_2O_4$ catalyst for gas-phase oxidation of ethanol to acetaldehyde. *J Am Chem Soc* 2013;135:14032-5. DOI PubMed
35. Wang G, Ling Y, Wheeler DA, et al. Facile synthesis of highly photoactive α-Fe_2O_3-based films for water oxidation. *Nano Lett* 2011;11:3503-9. DOI PubMed
36. Abraham KM, Chaudhri SM. The lithium surface film in the Li/SO_2 cell. *J Electrochem Soc* 1986;133:1307-11. DOI
37. Benoist L, Gonbeau D, Pfister-Guillouzo GP, Schmidt E, Meunier G, Levasseur A. XPS analysis of oxido-reduction mechanisms during lithium intercalation in amorphous molybdenum oxysulfide thin films. *Solid State Ionics* 1995;76:81-9. DOI
38. Liang Y, Wang H, Zhou J, et al. Covalent hybrid of spinel manganese-cobalt oxide and graphene as advanced oxygen reduction electrocatalysts. *J Am Chem Soc* 2012;134:3517-23. DOI PubMed
39. Xu Y, Wang X, Chen H, Kuang D, Su C. Toward high performance photoelectrochemical water oxidation: combined effects of ultrafine cobalt iron oxide nanoparticle. *Adv Funct Mater* 2016;26:4414-21. DOI
40. Nie R, Shi J, Du W, Ning W, Hou Z, Xiao F. A sandwich N-doped graphene/Co_3O_4 hybrid: an efficient catalyst for selective oxidation of olefins and alcohols. *J Mater Chem A* 2013;1:9037-45. DOI
41. Kim H, Park J, Park I, et al. Coordination tuning of cobalt phosphates towards efficient water oxidation catalyst. *Nat Commun* 2015;6:8253. DOI PubMed PMC
42. He B, Jia S, Zhao M, et al. General and robust photothermal-heating-enabled high-efficiency photoelectrochemical water splitting. *Adv Mater* 2021;33:e2004406. DOI PubMed
43. Zhang Y, Liu Y, Gong X, et al. Construction of piezoelectric photocatalyst Au/$BiVO_4$ for efficient degradation of tetracycline and studied at single-particle level. *Chem Synth* 2024;4:21. DOI
44. Tong M, Wang T, Lin S, et al. Ultra-thin carbon doped TiO_2 nanotube arrays for enhanced visible-light photoelectrochemical water splitting. *Appl Surf Sci* 2023;623:156980. DOI
45. Tong MH, Chen YX, Wang TM, et al. Cerium synchronous doping in anatase for enhanced photocatalytic hydrogen production from ethanol-water mixtures. *Molecules* 2023;28:2433. DOI PubMed PMC
46. Jiang X, Zhou J, Liu H, Chen Y, Lu C. Lotus pollen-templated synthesis of C, N, P-self doped $KTi_2(PO_4)_3/TiO_2$ for sodium ion battery. *Colloid Surface A* 2022;650:129605. DOI
47. Zhou Q, Chen Y, Shi H, et al. The construction of p/n-Cu_2O heterojunction catalysts for efficient CO_2 photoelectric reduction. *Catalysts* 2023;13:857. DOI
48. Tong M, Chen Y, Lin S, et al. Synchronous electrochemical anodization: a novel strategy for preparing cerium doped TiO_2 nanotube arrays toward visible-light PEC water splitting. *Electrochim Acta* 2023;463:142793. DOI
49. Zhang Y, Xu L, Liu B, et al. Engineering $BiVO_4$ and oxygen evolution cocatalyst interfaces with rapid hole extraction for photoelectrochemical water splitting. *ACS Catal* 2023;13:5938-48. DOI
50. Xiao J, Fan L, Huang Z, et al. Functional principle of the synergistic effect of co-loaded Co-Pi and FeOOH on Fe_2O_3 photoanodes for photoelectrochemical water oxidation. *Chinese J Catal* 2020;41:1761-71. DOI
51. Hu Z, Wang R, Han C, Chen R. Plasmon-induced hole-depletion layer on p-n heterojunction for highly efficient photoelectrochemical water splitting. *J Colloid Interface Sci* 2022;628:946-54. DOI PubMed